Low Temperature Physics/Fizika Nizkikh Temperatur, 2019, v. 45, No. 8, pp. 1018–1028

Electronic structure, Fermi surface and x-ray magnetic circular dichroism in the $CeAgSb_2$

V.N. Antonov

G.V. Kurdyumov Institute for Metal Physics of the NAS of Ukraine, 36 Vernadsky Str., Kiev 03142, Ukraine
E-mail: antonov@imp.kiev.ua

Received December 22, 2018, published online June 26, 2019

The electronic structure, Fermi surface, angle dependence of the cyclotron masses and extremal cross sections of the Fermi surface as well as x-ray magnetic circular dichroism (XMCD) in the $CeAgSb_2$ compound were investigated from first principles using the fully relativistic Dirac linear muffin-tin orbital method. In our calculations Ce 4*f* states have been considered as: 1) itinerant using the generalized gradient approximation (GGA), 2) fully localized, treating them as core states, and 3) partly localized using the GGA+*U* approximation. The effect of the spin-orbit (SO) interaction and Coulomb repulsion *U* in a frame of the GGA+*U* method on the Fermi surface, orbital dependence of the cyclotron masses, and extremal cross sections of the Fermi surface are examined in details. We show that the conventional GGA band calculations fail to describe the Fermi surface of the $CeAgSb_2$ due to wrong position of Ce 4*f* states (too close to the E_F). On the other hand, fully localized (4*f* states in core) and the GGA+ *U* approach produce similar Fermi surfaces and dHvA frequencies in the $CeAgSb_2$. A good agreement with the experimental data of XMCD spectra at the Ce $M_{4,5}$ edges was achieved using the GGA+*U* approximation. The origin of the XMCD spectra in the compound is examined. The core hole effect in the final states has been investigated using a supercell approximation. It improves the agreement between the theory and the experiment of the XAS and the XMCD spectra at the Ce $M_{4,5}$ edges.

Keywords: Fermi surface, magnetic circular dichroism, electronic structure.

The study of quantum many-body systems has witnessed tremendous progress fostered by impressive advances in the manufacturing of novel materials, their accurate probing at the quantum level and their characterization with sophisticated numerical simulations. One of the most striking discoveries in recent years are unconventional quantum phases of matter including topological insulators [6–10], Weyl semimetals [11–13], and quantum spin liquids (QSL) [8,14–17]. Topological insulators are fully gapped in the bulk but, due to strong spin-orbit coupling, possess metallic surface states that are protected by time-reversal symmetry [1,18]. In a QSL, strong quantum fluctuations prevent long-range magnetic order and instead a non-trivial ground state forms with long-range quantum entanglement between spins [19,20]. The paramount attention given to such states can be understood by the fact that they are topologically protected from decoherence [21], display fractional excitations with Majorana statistics, and therefore hold promise in the field of quantum information and quantum computation [22–24].

From a fundamental and theoretical perspective a special role is reserved to quantum phase transitions (QPTs) [25]. The nature of QPTs is fundamentally different from that of classical phase transitions at finite temperatures because the former is driven not by thermal fluctuations but by quantum fluctuations [26]. Ce- and Yb-based 4*f*-electron systems are particularly suited for investigating the QPTs because the energy scale of the magnetic interaction in these systems is quite small (~ 10 K); thus, their magnetic ground states can be easily modified by control parameters such as pressure, magnetic field, or doping. The physical properties are markedly affected by quantum fluctuations around quantum critical points (QCPs) and often show deviations from the Landau–Fermi liquid behavior [27].

In rare-earth compounds, where 4*f* levels are relatively close to the Fermi energy, various anomalous phenomena frequently appear. Most of them can be attributed to the hybridization between the 4*f* states and conduction bands. The great interest for the electronic and magnetic structures in compounds formed between rare-earth (*R*) and transition metals (*T*) has been recognized for a long time. However, among the *R*, cerium is somehow a controversial element. In cerium metal the 4*f* states are at the borderline between localized and itinerant behavior. This is reflected

in a remarkable transition from the fcc γ phase with localized 4*f* configuration into the isostructural α phase with delocalized 4*f* configuration. The transition may be driven thermally, by the application of pressure or by alloying and formation of compounds with *d*-band transition metals, and is initially related to a varying degree of mixing of the 4*f* and conducting states i.e., to the formation of highly correlated electronic structure.

The intermetallic $CeAgSb_2$ belongs to the $CeTSb_2$ family (T = Au, Ag, Pd, Cu) which form dense Kondo systems in the $ZrCuSi_2$ type structure (space group $P4/nmm$) [28,29]. The nature of the magnetic ordering of the $CeAgSb_2$ remained controversial until neutron scattering revealed that the ordered phase is ferromagnetic (FM). The magnetic moments, originating from the Ce atoms, are aligned along the *c* axis with an ordered moment of $\mu = 0.4\mu_B$/Ce below the Curie temperature T_C = 9.6 K [29]. The magnetic properties of this compound are unusual. For example, the magnetization perpendicular to the *c*-axis in the FM state increases almost linearly with the magnetic field up to around 3 T, reaching $\sim 1.2\ \mu_B$/Ce [25]. The induced magnetic moment above 3 T is considerably larger than the spontaneous magnetic moment in the FM state. Moreover, in the paramagnetic state, the magnetic susceptibility perpendicular to the *c*-axis is larger than that along the *c*-axis, except in the critical region.

Logg *et al.* [30] have investigated the sensitivity of the FM phase of the $CeAgSb_2$ to hydrostatic pressure and a transverse magnetic tuning field using a series of resistivity and magnetization measurements. With pressure, T_C is suppressed rapidly, and extrapolates to zero at 35 kbar. The application of an in-plane tuning field similarly suppresses T_C, and drives the transition to zero temperature by 2.8 T. The character of the phase transition remains continuous on the approach to T = 0 K, and it is found that the quadratic-coefficient from the resistivity is strongly enhanced near the critical field. Kawasaki *et al.* [25] investigated the magnetic properties of the $CeAgSb_2$ performing dc-magnetization and ac-susceptibility measurements. They found that the Curie temperature is suppressed to zero by the application of H_{ab}, and the ac-susceptibility measured along the *c*-axis under H_{ab} continuously shows a critical-divergence-like anomaly at T_C, indicating the presence of a field-induced ferromagnetic quantum critical point in this compound. The electronic specific heat coefficient γ of single-crystal [31] $CeAgSb_2$ is 65 mJ·K·mol^{-1} indicative of heavy mass carriers. Measurements of the de Haas-van Alphen (dHvA) effect have been used by Inada *et al.* [32] to study the Fermi surface of the $CeAgSb_2$. The dHvA frequencies were between 41 T and 120 kT. The Shubnikov–de Haas (SdH) measurement has been reported by Myers *et al.* [33] for magnetic field parallel to the *c*-axis. A single orbit of ~ 25 T has been observed at 1.2 kbar at 2.1 K. Jobiliong *et al.* [34] also provide the SdH measurements in the $CeAgSb_2$. They found, in agreement with previous measurements of Myers *et al.* [33], that a small (25 T) orbit dominates the SdH signal, indicating significant differences between the SdH and previous dHvA results where no frequency below 40 T was observed [32].

Saitoh *et al.* [35] report a combined study on the electronic structures of FM $CeAgSb_2$ using soft x-ray absorption (XAS), magnetic circular dichroism (XMCD), and angle-resolved photoemission (ARPES) spectroscopies. The Ce $M_{4,5}$ XAS spectra show satellite structures, reflecting a strongly localized character of the Ce 4*f* electrons. Nevertheless, ARPES spectra at the Ce 3*d*–4*f* resonance show the momentum dependence of the intensity ratio between Ce $4f_{5/2}$ peaks in a part of the Brillouin zone, suggesting the non negligible momentum-dependent hybridization effect between the Ce 4*f* and the conduction electrons. This is associated with the moderate mass enhancement in the $CeAgSb_2$. It is in contradiction with low temperature dHvA experiments for fields along the *c* axis which show large cylindrical Fermi surfaces with extremely large cyclotron masses of 0.85–32 m_e [32].

The energy band structure calculations of the $CeAgSb_2$ presented in Ref. 32 have been carried out in the local density approximation (LDA) without taken into account strong Coulomb correlations. However, some experiments point out on strong localization of the Ce 4*f* states in the $CeAgSb_2$. Clear crystalline electric-field (CEF) excitations were observed in neutron scattering experiments, indicating a localized character of the Ce 4*f* electrons [29]. This assertion has also been supported by a high-field magnetization study [36]. The XMCD results presented by Saitoh *et al.* [35] give support to the picture of local-moment magnetism in the $CeAgSb_2$. Moreover, it was also found that the theoretical band dispersions for $LaAgSb_2$ provide a better description of the ARPES band structures than those for $CeAgSb_2$. We can conclude that due to strong localization of Ce 4*f* states the Hubbard type Coulomb correlations have to be included in the calculation of the electronic structure and physical properties of the $CeAgSb_2$.

Here we present comprehensive theoretical calculations of the electronic structure, Fermi surface properties as well as XAS and XMCD spectra of the $CeAgSb_2$. The energy band structure of the $CeAgSb_2$ in this paper is calculated within the *ab initio* approach by applying the generalized gradient approximation (GGA) using the fully relativistic spin-polarized Dirac linear muffin-tin orbital band-structure method with taking into account strong electron-electron correlations.

The paper is organized as follows. The computational details are presented in Sec. 2. Section 3 presents the electronic structure of the $CeAgSb_2$ compound. Section 4 is devoted to the Fermi surface, angle dependence of the cyclotron masses and extremal cross sections of the Fermi surface in the $CeAgSb_2$ treating the Ce 4*f* states as: (1) itinerant using the GGA, (2) fully localized, treating them

as core states, and (3) partly localized using the GGA+U approximation. Section 5 presents the theoretically calculated XAS and XMCD spectra of the $CeAgSb_2$ compound at Ce $M_{4,5}$ edges, theoretical results are compared with the experimental measurements. Finally, the results are summarized in Sec. 4.

2. Computational details

2.1. Crystal structure

The intermetallic $CeAgSb_2$ belongs to the $CeTSb_2$ family (T = Au, Ag, Pd, Cu) which form dense Kondo systems in the $ZrCuSi_2$ type structure [28,29]. Figure 1 presents schematically the crystal structure of the tetragonal $CeAgSb_2$ (the space group is $P4/nmm$, No. 129). Blue spheres represent Ce atoms, green spheres are Ag atoms, red and magenta spheres show Sb atoms. In this structure, Ce atoms show a quasi-body-centered tetragonal lattice. The local arrangements of Ce and Sb atoms are very similar to those of $CeSb_2$. In the $CeAgSb_2$, the $CeSb_2$ layer is separated by an Ag layer [29]. Table 1 presents atomic positions and lattice constants of the tetragonal $CeAgSb_2$ used in our band structure calculations. Ce has four Ag neighbors at the 3.5485 Å distance, four Sb1 neighbors at the 3.3626 Å distance, and four Sb2 neighbors at the 3.228 Å distance. Ag is surrounded has four Sb2 neighbors at the 2.8664 Å distance, four Ag atoms at the 3.0883 Å distance and four Ce atoms at the 3.5485 Å distance.

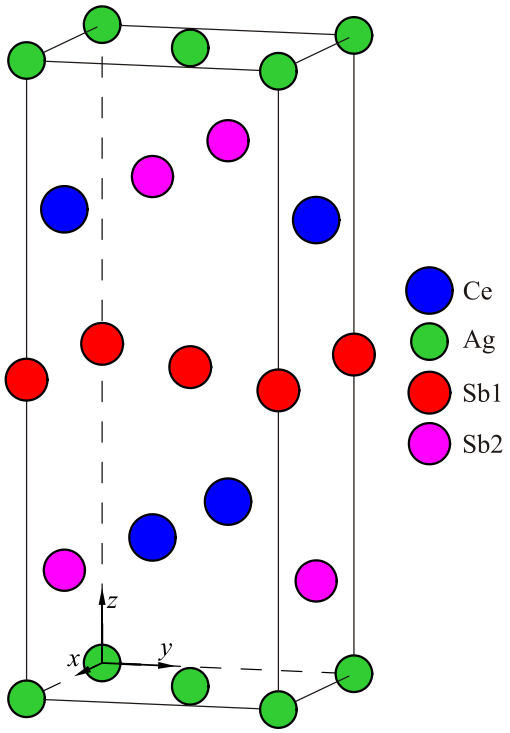

Fig. 1. (Color online) Crystal structure of the tetragonal $CeAgSb_2$ (the space group is $P4/nmm$, No. 129). Blue spheres represent Ce atoms, green spheres are Ag atoms, red and magenta spheres show Sb atoms.

Table 1. Structural parameters of the tetragonal $CeAgSb_2$. The space group is $P4/nmm$ (No. 129) and the lattice constants are a = 4.3675 Å and c = 10.708 Å; x, y, z denote Wyckoff positions [29]

Atom	Site	x	y	z
Ce	2c	1/4	1/4	0.2388
Ag	2b	3/4	1/4	1/2
Sb1	2a	3/4	1/4	0
Sb2	2c	1/4	1/4	0.6734

Araki *et al.* [29] neutron-scattering study of the crystal structure of the $CeAgSb_2$ revealed crystalline electric-field level scheme, which consists of the $|\pm\frac{1}{2}\rangle$ ground state and the first and second excited levels dominated by $|\pm\frac{3}{2}\rangle$ and $|\pm\frac{5}{2}\rangle$, respectively. The spatial distribution of the ground-state Ce 4f wave function with $|\pm\frac{1}{2}\rangle$ symmetry is oriented along the c-axis and each Ce atom has no neighboring atoms along the c-axis, as shown in Fig. 1. Therefore, the essentially localized nature of the 4f electrons in the $CeAgSb_2$ can be understood as a natural consequence of the local atomic environment [25].

2.2. X-ray magnetic circular dichroism

Magneto-optical (MO) effects refer to various changes in the polarization state of light upon interaction with materials possessing a net magnetic moment, including rotation of the plane of linearly polarized light (Faraday, Kerr rotation), and the complementary differential absorption of left and right circularly polarized light (circular dichroism). In the near visible spectral range these effects result from excitation of electrons in the conduction band. Near x-ray absorption edges, or resonances, magneto-optical effects can be enhanced by transitions from well-defined atomic core levels to transition symmetry selected valence states.

Within the one-particle approximation, the absorption coefficient $\mu_j^{\lambda}(\omega)$ for incident x-ray of polarization λ and photon energy $\hbar\omega$ can be determined as the probability of electronic transitions from initial core states with the total angular momentum j to final unoccupied Bloch states

$$\mu_j^{\lambda}(\omega) = \sum_{m_j}\sum_{n\mathbf{k}} |\langle \Psi_{n\mathbf{k}} | \Pi_{\lambda} | \Psi_{jm_j} \rangle|^2 \, \delta(E_{n\mathbf{k}} - E_{jm_j} - \hbar\omega) \times$$

$$\times \, \theta(E_{n\mathbf{k}} - E_F), \qquad (1)$$

where Ψ_{jm_j} and E_{jm_j} are the wave function and the energy of a core state with the projection of the total angular momentum m_j; $\Psi_{n\mathbf{k}}$ and $E_{n\mathbf{k}}$ are the wave function and the energy of a valence state in the n-th band with the wave vector k; E_F is the Fermi energy.

Π_λ is the electron-photon interaction operator in the dipole approximation

$$\Pi_\lambda = -e\boldsymbol{\alpha}\,\mathbf{a}_\lambda, \tag{2}$$

where $\boldsymbol{\alpha}$ are the Dirac matrices, and $\mathbf{a}_\lambda$ is the λ polarization unit vector of the photon vector potential, with $a_\pm = 1/\sqrt{2}(1,\pm i,0)$, $a_\| = (0,0,1)$. Here, + and – denotes, respectively, left and right circular photon polarizations with respect to the magnetization direction in the solid. Then, x-ray magnetic circular and linear dichroism are given by $\mu_+ - \mu_-$ and $\mu_\| - (\mu_+ + \mu_-)/2$, respectively. More detailed expressions of the matrix elements in the electric dipole approximation may be found in Refs. 37–40. The matrix elements due to magnetic dipole and electric quadrupole corrections are presented in Ref. 40.

Concurrent with the development of the x-ray magnetic circular dichroism experiment, some important magneto-optical sum rules have been derived [41–46].

For the $L_{2,3}$ edges the l_z sum rule can be written as [39]

$$\langle l_z \rangle = n_h \frac{4}{3} \frac{\int_{L_3+L_2} d\omega(\mu_+ - \mu_-)}{\int_{L_3+L_2} d\omega(\mu_+ + \mu_-)}, \tag{3}$$

where n_h is the number of holes in the d band $n_h = 10 - n_d$, and $\langle l_z \rangle$ is the average of the magnetic quantum number of the orbital angular momentum. The integration is taken over the whole $2p$ absorption region. The s_z sum rule can be written as

$$\langle s_z \rangle + \frac{7}{2}\langle t_z \rangle = $$

$$= n_h \frac{\int_{L_3} d\omega(\mu_+ - \mu_-) - 2\int_{L_2} d\omega(\mu_+ - \mu_-)}{\int_{L_3+L_2} d\omega(\mu_+ + \mu_-)}, \tag{4}$$

where t_z is the z component of the magnetic dipole operator $\mathbf{t} = s - 3\mathbf{r}(\mathbf{r}\cdot\mathbf{s})/|\mathbf{r}|^2$ which accounts for the asphericity of the spin moment. The integration $\int_{L_3}\left(\int_{L_2}\right)$ is taken only over the $2p_{3/2}$ $(2p_{1/2})$ absorption region.

2.3. Calculation details

The details of the computational method are described in our previous papers [47–49] and here we only mention several aspects. Band structure calculations were performed using the fully relativistic linear muffin-tin orbital (LMTO) method [50,51]. This implementation of the LMTO method uses four-component basis functions constructed by solving the Dirac equation inside an atomic sphere [52]. The exchange-correlation functional of a GGA-type was used in the version of Perdew, Burke and Ernzerhof (PBE) [53]. Brillouin zone (BZ) integration was performed using the improved tetrahedron method [54]. For obtaining the self-consistent solution we used 216 **k** points in the irreducible part of the BZ. In order to obtain an accurate shape of the Fermi surface, we used extended mash with 102425 **k** points in the irreducible part of the BZ. The basis consisted of Ce Ag, and Sb s, p, d, and f LMTO's.

To take into account electron-electron correlation effects, we used in this work the "relativistic" generalization of the rotationally invariant version of the LSDA+U method [55], which takes into account SO coupling so that the occupation matrix of localized electrons becomes non-diagonal in spin indexes. This method is described in detail in our previous paper [55], including the procedure to calculate the screened Coulomb U and exchange J integrals, as well as the Slater integrals F^2, F^4, and F^6.

The screened Coulomb U and exchange Hund coupling J_H integrals enter the LSDA+U energy functional as external parameters and have to be determined independently. These parameters can be determined from supercell LSDA calculations using Slater's transition state technique [56,57], from constrained LSDA calculations (cLSDA) [57–61], or from the constrained random-phase approximation (cRPA) scheme [62]. Subsequently, a combined cLSDA and cRPA method was also proposed [63]. The cLSDA calculations produce J_H = 0.85 eV for the Ce site in the $CeAgSb_2$. It is known, that the cRPA method underestimates values of U in some cases [64]. On the other hand, the cLSDA method produces too large values of U [65]. Therefore, in our calculations we treated the Hubbard U as an external parameter and varied it from 2.0 to 7.0 eV. We found relatively small sensitivity of the Ce $M_{4,5}$ XAS and XMCD spectra on precious value of Hubbard U. We used the value U = 6.0 eV in our calculations which is typical for 4f correlated systems [39].

The x-ray absorption and dichroism spectra were calculated taking into account the exchange splitting of core levels. The finite lifetime of a core hole was accounted for by folding the spectra with a Lorentzian. The widths of core level spectra $\Gamma_{M_{4,5}}$ for Ce were taken from Ref. 66. The finite experimental resolution of the spectrometer was accounted for by a Gaussian of width 0.6 eV.

3. Electronic structure

The 4f-electron lanthanide compounds are usually treated by a 4f-localized model (4f electrons in core). The localized 4f-electron picture is a good starting point in description of the electronic structure of lanthanides. On the other hand, there are several interesting phenomena such as metal–insulator transitions, valence fluctuations in the Kondo effect, heavy fermion behavior, superconductivity, and so on. All these effects strongly depend on the hybridization between 4f and conduction electrons and cannot be described correctly in the 4f-localized model.

An important issue is the energy position of the Ce 4f states in the electron band structure of the $CeAgSb_2$. It is well known that LDA (as well as GGA) usually gives a

wrong energy position for the 4*f* states in rare-earth compounds. For nonzero 4*f* occupation it places the 4*f* states right at the Fermi level [39] in contradiction to various experimental observations.

Figure 2 shows the *ab initio* fully relativistic energy band structure of the $CeAgSb_2$. In these calculations the 4*f* states have been considered as: (1) itinerant using the generalized gradient approximation, (2) fully localized, treating them as core states, and (3) partly localized using the GGA+*U* approximation. The GGA approach places Ce 4*f* states in the $CeAgSb_2$ at the Fermi level (upper panel of Fig. 2) with Ce 4*f* occupation equal to 0.96 and 0.32 electrons for spin-up and spin-down state, respectively. The GGA magnetic moments are equal to 0.33, –0.75, and –0.42 for spin M_s, orbital M_l, and total M_{total}, respectively. The conduction electrons in the $CeAgSb_2$ are mainly due to Sb 5*p*, Sb 5*d*, Ce 5*d* and Ce 4*f* electrons. Their contributions to the density of states at the Fermi energy are 2.7%, 1.5%, 1.5%, and 93.2%, respectively. The contribution of the 4*f* electron is dominant at the Fermi energy in the itinerant picture of the GGA approach.

The applying of the GGA+*U* approach results in a correlation correction to the mean-field approximation of the self-energy with the shift of the occupied Ce 4*f* states by $U_{\text{eff}}/2$ downward below the Fermi level and empty states by $U_{\text{eff}}/2$ upward above the Fermi level, respectively (lower panel of Fig. 1). As a result, occupied Ce 4*f* level is situated at –2.4 eV below the Fermi level, empty Ce 4*f* are at 2 to 4 eV above the Fermi level. We can conclude that the Kondo lattice scenario is appropriate for $CeAgSb_2$ compound, because for a Kondo resonance to develop both the occupied and empty 4*f* states must be sufficiently far away from the Fermi level. Indeed, $CeAgSb_2$ manifests a temperature-dependent resistivity typical of a Kondo lattice [33].

It is interesting to note that the GGA+*U* approach and the fully localized model with 4*f* in core produce almost identical energy bands in close vicinity of the Fermi level (comparer color bands in the middle and lower panels of Fig. 2). These two approaches produce similar Fermi surfaces of the $CeAgSb_2$. We found also that the theoretical band dispersions in the GGA+*U* approximation for $CeAgSb_2$ provide a better description of the ARPES band structure [35] than those for the GGA approach.

Figure 3 presents the total and partial density of states of the $CeAgSb_2$. The Ag 4*d* states are located far below

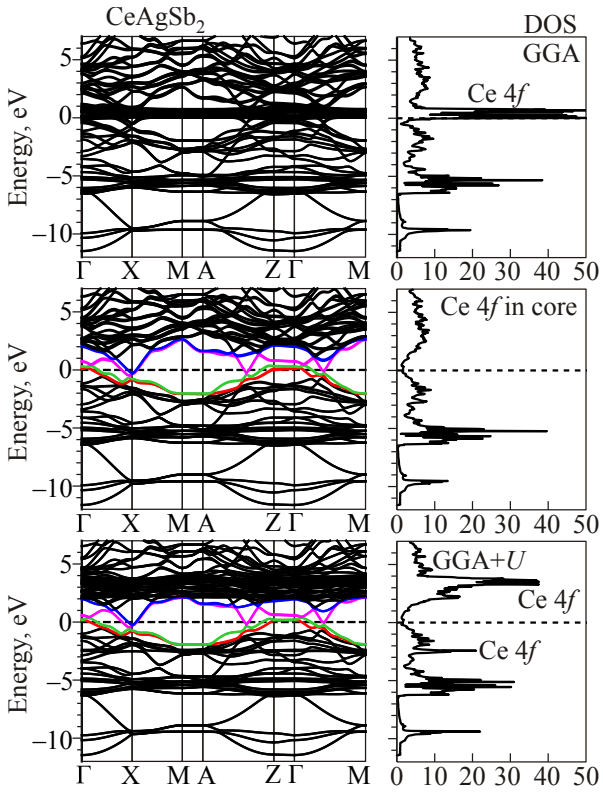

Fig. 2. (Color online) Self-consistent fully relativistic, spin-polarized energy band structure and total DOS (in states/(unit cell eV)) calculated for $CeAgSb_2$ treating Ce 4*f* states as: (1) itinerant in the GGA approximation (upper panel); (2) fully localized with 4*f* in core (middle panel); and (3) partly localized in the GGA+*U* approach (lower panel).

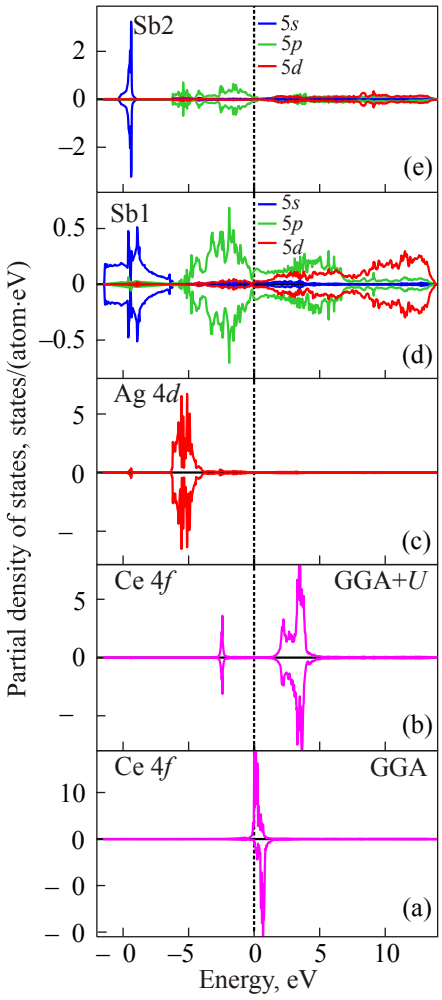

Fig. 3. (Color online) The partial DOSs of the $CeAgSb_2$ calculated in the GGA+*U* approximation with U_{eff} = 5.1 eV. The lower panel presents Ce 4*f* partial DOS in the GGA approach.

the Fermi level between –6.6 and –3.9 eV. The 5*s* states of Sb_1 and Sb_2 sites have significantly different shape in different energy range. There is a large energy gap between 5*s* and 5*p* states at the Sb1 site, the corresponding gap is much smaller for the Sb2 site.

4. Fermi surface

In the absence of magnetic field in the fully relativistic Dirac representation, due to the time-reversal symmetry, all bands of the $CeAgSb_2$ are at least twofold degenerate. A small FM moment $0.4\mu_B$ at the Ce atom lifts the degeneracy. The spin splitting effect for conduction electrons with degenerated up- and down-spin states can be reasons why each dHvA branch consists of a few branches [32].

In the following analysis, to distinguish individual bands it will be convenient to keep the numeration of the bands by spin-splitted pairs, adding a subscript if necessary. There are four spin-splitted pairs of energy bands cross the Fermi energy (E_F). We will number these bands as the $1_{1,2}$-st, $2_{1,2}$-nd, $3_{1,2}$-rd, and $4_{1,2}$-th bands. They present in Fig. 1 and have red, green, magenta, and blue colors, respectively. Similar colors will be used for the presentation of the corresponding Fermi surface cross-sections (Fig. 4) as well as the theoretically calculated dHvA oscillations in the $CeAgSb_2$ (Fig. 6).

Relevant features of the energy bands in the GGA+*U* approximation, presented in Fig. 2(c), include two band crossings of the E_F near the Γ point, the two band crossings E_F near the *X* point, one crossing along *A*–*Z* and one along Γ–*M* directions. Figure 4 presents the calculated Fermi surface cross section areas of the $CeAgSb_2$ in the plane perpendicular to the k_z direction and cross Γ symmetry point (k_z = 0, Γ*XMX* plane) for non-magnetic (a) and FM ordered (b) solutions using the fully relativistic Dirac GGA approximation. The Figure 4(c) shows the calculated Fermi surface cross section areas for ferromagnetic $CeAgSb_2$ in the GGA+*U* approach. The FM ordering as well as Coulomb correlations significantly influence the theoretically calculated Fermi surfaces of the $CeAgSb_2$. The cross sections of the $CeAgSb_2$ FS in the GGA+*U* approximation presented in Fig. 4(c) is in good agreement with the ARPES measurement [67].

The temperature dependence of the resistivity in high quality monocrystal of the $CeAgSb_2$ have been measured by Inada *et al.* [68]. They found a very large anisotropy of the resistivity: the ratio between $J \parallel [001]$ and [100] is 8.3 at room temperature and 17 around 10 K, reflecting the quasi-two dimensional electronic states in the $CeAgSb_2$. Ferromagnetic $CeAgSb_2$ have a hollow cylindrical Fermi surface as shown in Fig. 5 due to possession a characteristic tetragonal crystal structure ($P4/nmm$) with the stacking arrangement of CeSb–Ag–CeSb–Sb layers along the [001] direction (*c*-axis) [32]. It brings about a flat Brillouin zone and produces cylindrical but corrugated Fermi surfaces

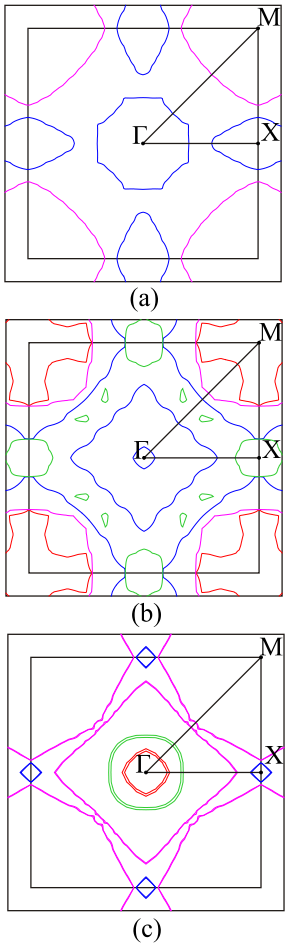

Fig. 4. (Color online) (a) The calculated Fermi surface cross-section areas of the $CeAgSb_2$ in the plane perpendicular to the *z* direction and cross Γ symmetry point in non-magnetic fully relativistic Dirac GGA approximation; (b) the calculated Fermi-surface cross-section areas in ferromagnetically ordered $CeAgSb_2$ in the GGA approximation; (c) the calculated Fermi-surface cross-section areas of ferromagnetic $CeAgSb_2$ in the GGA+*U* approach.

along [001]. There are four sheets of the FS in the GGA+*U* calculations. The first and the second energy bands produce two hole sheets around Γ symmetry point [Figs. 5(a), (b)] with a weak dispersion along the k_z direction. The third energy band produces a large open electron FS [Fig. 5(c)]. The fourth energy band creates a small closed electron FS centered at the *X* symmetry point [Fig. 5(d)].

Figure 6 presents the angular variations of the theoretically calculated dHvA frequencies in the $CeAgSb_2$ in the GGA+*U* approximations for field direction in the (101) plane in comparison with the experimentally measured frequencies (full black squares) [32]. The dHvA frequency $F = 2\pi e/\hbar c S_F$ is proportional to the extremal (maximum or minimum) cross-sectional area of the Fermi surface S_F [69]. We can assumed that all the dHvA branches correspond to cylindrical Fermi surfaces because the dHvA frequencies follow the $1/\cos\theta$-dependence, where θ is a tilted field angle from [001] to [100] direction.

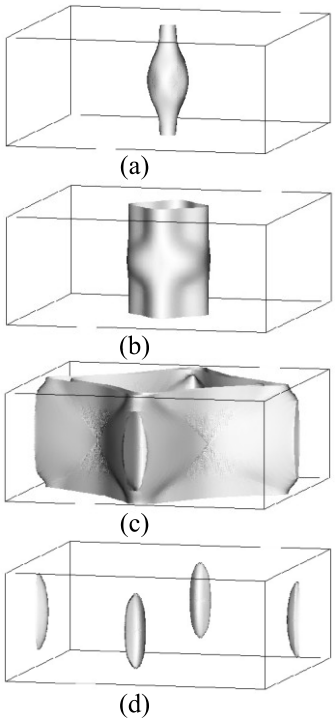

Fig. 5. (Color online) The theoretically calculated first hole (a), second hole (b), third electron (c), and fourth electron (d) Fermi surfaces of the $CeAgSb_2$ in the GGA+U approximation.

There are two groups of dHvA frequency branches were observed at high magnetic field ranging from 41 T to 11.2 kT (low frequencies) and between 70 and 120 kT (high frequencies) [32]. The high frequency branches correspond entirely to the large open electron FS [Fig. 5(c)]. However, all four sheets of the FS contribute to the low frequency oscillations (Fig. 6). The theory quite well reproduces the angle dependence of the experimentally measured dHvA oscillations.

We should mention that the Shubnikov–de Haas measurement [33,34] observe an additional small (25 T) orbit, indicating significant differences between the SdH and previous dHvA results where no frequency below 40 T was observed [32]. We also found two extremal cross-sectional areas of the Fermi surface S_F in vicinity of [001] direction with values of 17–19 and 21–23 T (see insert in Fig. 6). They correspond to the first and second hole Fermi surface sheets [Figs. 5(a), (b)] derived from the energy band crossing the E_F near Γ symmetry point.

We found also that the GGA approximation produces the Fermi surface and dHvA frequencies in inadequate agreement with the experimental measurements (see Fig. 7) due to wrong position of Ce 4*f* states (too close to the E_F).

The theoretically calculated cyclotron masses in the $CeAgSb_2$ in the GGA+U approximation present in Fig. 8. Open red, green, magenta, and blue circles correspond to the 1-hole, 2-hole, 3-electron, and 4-electron Fermi surfaces, respectively. We found that the theoretically calculated cyclotron masses are rather small and do not exceeded the value of $\pm 1.0 m_e$. However, the dHvA measurements produce extremely large cyclotron masses m_c^* of 0.85–32 m_e [32], roughly one order of magni-

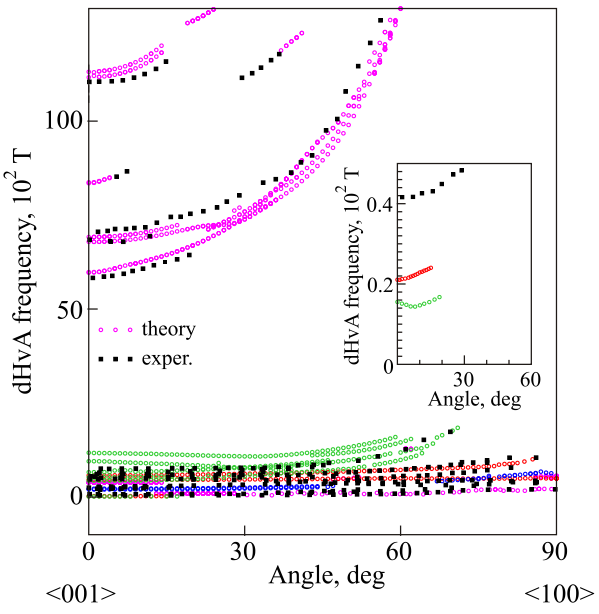

Fig. 6. (Color online) The experimentally measured [32] (full black squads) dependences of the dHvA oscillation frequencies in the $CeAgSb_2$ in comparison with theoretically calculated ones in the GGA+U approximation. Open red, green, magenta, and blue circles correspond to the extremal cross-sections of the 1-hole, 2-hole, 3-electron, and 4-electron Fermi surfaces, respectively.

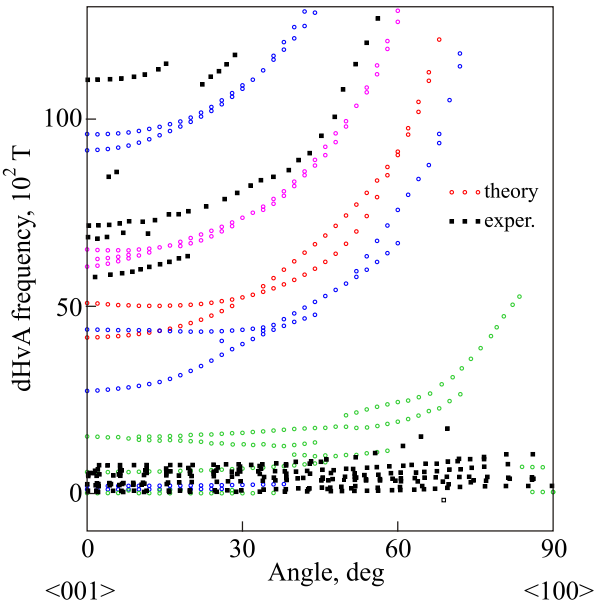

Fig. 7. (Color online) The experimentally measured [32] (full black squares) dependences of the dHvA oscillation frequencies in the $CeAgSb_2$ in comparison with theoretically calculated ones in the GGA approximation.

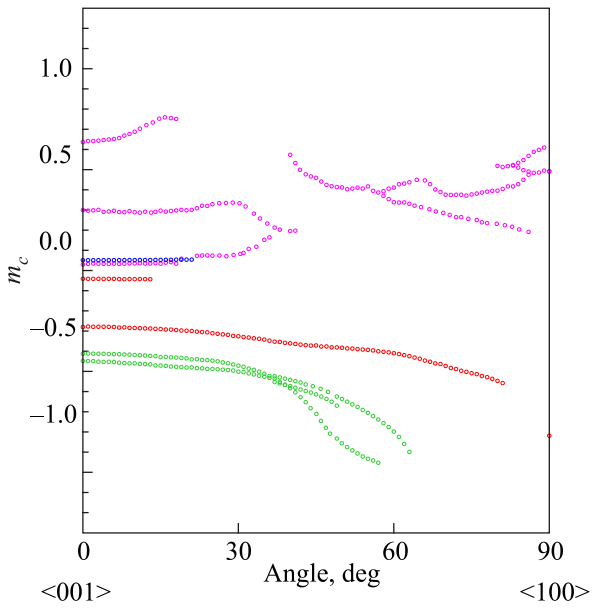

Fig. 8. (Color online) The theoretically calculated cyclotron masses (in m_e) in the $CeAgSb_2$ in the GGA+U approximation. Open red, green, magenta and blue circles correspond to the 1-hole, 2-hole, 3-electron, and 4-electron Fermi surfaces, respectively.

tude larger than the band cyclotron mass. It should be mentioned that the mass enhancement based on the many-body Kondo effect is not included in the conventional band structure calculations. It is caused by spin fluctuations, where the freedom of the charge transfer of 4*f*-electrons appear in the form of an 4*f*-itinerant band, but the freedom of spin fluctuations of the same 4*f*-electrons reveals a relatively small magnetic moment and enhances the effective mass. Therefore, the present mass enhancement may be attributed to the Kondo effect. The electron-phonon interaction is also contributed to the cyclotron mass enhancement [39].

On the other hand, several other experiments on the Fermi surface of the $CeAgSb_2$ reveal much smaller cyclotron masses in comparison with the dHvA measurements [32]. Prozorov *et al.* [70] measured SdH oscillations in single crystal of FM $CeAgSb_2$ using a tunnel diode resonator. Resistivity oscillations as a function of applied magnetic field were observed via measurements of skin depth variation. The temperature dependence of the amplitude of the SdH oscillations in the $CeAgSb_2$, taken for several single oscillations allows them to roughly estimate the effective mass of low frequency orbit as $m_c^* = 0.6\pm0.1 m_0$ [70]. Bud'ko *et al.* [71] measure effective masses using quantum oscillations in magnetostriction in $RAgSb_2$ (R = Y, Sm, La) single crystals which expected to have similar Fermi surfaces to the $CeAgSb_2$ one. They found that the effective masses were between 0.1 and $0.3 m_e$. Apparently, the question about effective masses in the $CeAgSb_2$ demands an additional experimental and theoretical attention.

5. IR $M_{4.5}$ x-ray absorption and XMCD spectra

The study of the 4*f* electron shell in rare-earth compounds is usually performed by tuning the energy of the x-ray close to the $M_{4.5}$ edges of rare earth where electronic transitions between $3d_{3/2.5/2}$ and $4f_{5/2.7/2}$ states are involved. Figure 9 shows the calculated XAS and XMCD spectra in the GGA+U approximation for the $CeAgSb_2$ at the $M_{4.5}$ edges together with the corresponding experimental spectra measured by Saitoh *et al.* [35]. The experimentally measured dichroism is large, as is common for *R*-based systems at the $3d$ threshold.

The theoretically calculated XAS spectra have a rather simple line shape composed of two white line peaks at the M_5 and M_4 edges. However the experimentally measured spectra have a well-known satellite situated at 4 eV below the main lines [35]. It was not produced by the theory because the multiplet structure has not been included in present calculations. From Fig. 9(a) one can see that the theory does not reproduce the experimentally observed M_5/M_4 XAS branching ratio. It is well known that in early $3d$ and

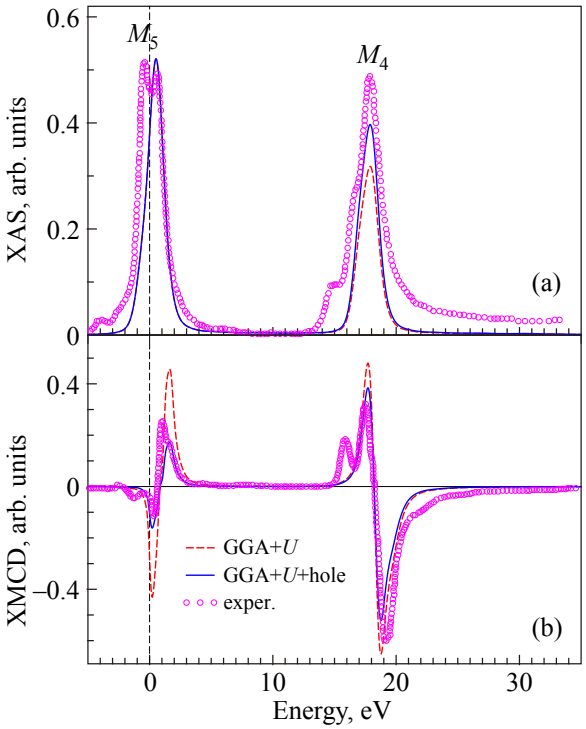

Fig. 9. (Color online) (a) Isotropic absorption spectra of the $CeAgSb_2$ at the Ce $M_{4.5}$ edges calculated by the GGA+U approximation without (dashed red lines) and with taking into account the core-hole effect (full blue lines) in comparison with the experimental data Ref. 35 (circles). Experimental spectra were measured with external magnetic field (10 T) at 6 K; (b) experimental (Ref. 35) XMCD spectra of the $CeAgSb_2$ at the Ce $M_{4.5}$ edges in comparison with theoretically calculated ones using the GGA+U approximation without (dashed red lines) and with (full blue lines) taking into account core-hole effect.

$4f$ metals with nearly empty $3d$ and $4f$ bands the $L_{2,3}$ and $M_{4,5}$ absorption channels are strongly coupled through the photoelectron core-hole Coulomb and exchange interactions [72–75]. This leads to a branching ratio of almost 1:1, far from the statistical ratio 2:1 and 3:2 for the L_3/L_2 and M_5/M_4, respectively, which is obtained in a single-particle theory-unless the spin-orbit interaction in the final $3d$ or $4f$ band is considered. From our relativistic band-structure calculations we obtained the M_5/M_4 branching ratio of 1.56.

We investigated the core-hole effect in the final state using the supercell approximation. When the $3d$ core electron is photoexcited to the unoccupied $4f$ states, the distribution of the charge changes to account for the created hole. To check the convergence of the XAS and XMCD spectra for the impurity site, we used supercell calculations with two and four formula units. Very similar spectra were obtained in both cases. The final-state interaction gives the M_5/M_4 branching ratio of 1.25, which is in better agreement with the experimental ratio.

As can be seen from Fig. 9(b) the GGA+U approximation describes quite well the shape of the XMCD spectra at the Ce $M_{4,5}$ edges. However it overestimates the intensity of the dichroic signal at the M_5 edge. It also fails to obtain small additional fine structures observed at the low-energy parts of the $M_{4,5}$ XMCD spectra. The final-state interaction improves the agreement between the theory and the experiment (full blue curves in the lower panel of Fig. 9).

Saitoh *et al.* [35] using sum rules obtained $M_{\text{total}} = 0.35\pm0.02$ μ_B/Ce and $M_l/M_s = -4.05\pm0.05$ μ_B/Ce from the XAS and XMCD spectra of the $CeAgSb_2$ at 6 K. Our GGA+U band structure calculations produce $M_{\text{total}} = 0.33$ μ_B/Ce and $M_l/M_s = -5.02$ μ_B/Ce in good agreement with the experimental data. The direct application of sum rules (Eqs. (3) and (4)) to the theoretically calculated spectra gives $M^{\text{sr}}_{\text{total}} = 0.37$ μ_B/Ce and $M_l/M_s = -3.92$.

6. Conclusions

The electronic structure, Fermi surface properties and x-ray magnetic circular dichroism of the $CeAgSb_2$ were investigated theoretically within a DFT in the frame of the fully relativistic spin-polarized Dirac LMTO band-structure method with taking into account Coulomb electron-electron correlations.

We found that the conventional GGA band calculations fail to describe the Fermi surface of the $CeAgSb_2$ due to wrong position of the $4f$ states (too close to the E_F). On the other hand, the GGA+U approach relatively well describes the Fermi surface of the $CeAgSb_2$. We can conclude that the inclusion of strong Coulomb repulsion in $4f$ shell is very important for the correct description of the Fermi-surface properties of the $CeAgSb_2$.

The theoretically calculated x-ray absorption spectra at the Ce $M_{4,5}$ edges have a rather simple line shape composed of two white line peaks with additional fine structures at the low-energy part of the spectra, which can be assigned to multiplet structures. The dichroism at the Ce $M_{4,5}$ edges is very large due to strong spin-orbit coupling of the initial Ce $3d$ core states and large spin polarization of the final empty $4f_{5/2,7/2}$ states. The core hole effect in the final states has been investigated using a supercell approximation. It improves the agreement between the theory and the experiment of the XAS and the XMCD spectra at the Ce $M_{4,5}$ edges.

Acknowledgments

The studies were supported by the National Academy of Sciences of Ukraine within the budget program KPKBK 6541230-1A “Support for the development of priority areas of scientific research”.

1. X.-L. Qi and S.-C. Zhang, *Phys. Today* **63**, 33 (2010).
2. Y. Ando, *J. Phys. Soc. Jpn*. **82**, 102001 (2013).
3. T.O. Wehling, A. Black-Schafferc, and A. Balatsky, *Adv. Phys*. **63**, 1 (2014).
4. A. Bansil, H. Lin, and T. Das, *Rev. Mod. Phys*. **88**, 021004 (2016).
5. V.N. Antonov, L.V. Bekenov, S. Uba, and A. Ernst, *Phys. Rev. B* **96**, 224434 (2017).
6. B.J. Kim, H. Jin, S.J. Moon, J.-Y. Kim, B.-G. Park, C.S. Leem, J. Yu, T.W. Noh, C. Kim, and S.-J. Oh, J.-H. Park, V. Durairaj, G. Cao, and E. Rotenberg, *Phys. Rev. Lett*. **101**, 076402 (2008).
7. B.J. Kim, H. Ohsumi, T. Komesu, S. Sakai, T. Morita, H. Takagi, and T. Arima, *Science* **323**, 1329 (2009).
8. G. Jackeli and G. Khaliullin, *Phys. Rev. Lett*. **102**, 017205 (2009).
9. H. Watanabe, T. Shirakawa, and S. Yunoki, *Phys. Rev. Lett*. **105**, 216410 (2010).
10. C. Martins, M. Aichhorn, L. Vaugier, and S. Biermann, *Phys. Rev. Lett*. **107**, 266404 (2011).
11. W. Witczak-Krempa and Y.B. Kim, *Phys. Rev. B* **85**, 045124 (2012).
12. A. Go, W. Witczak-Krempa, G.S. Jeon, K. Park, and Y.B. Kim, *Phys. Rev. Lett*. **109**, 066401 (2012).
13. A.B. Sushkov, J.B. Hofmann, G.S. Jenkins, J. Ishikawa, S. Nakatsuji, S. Das Sarma, and H.D. Drew, *Phys. Rev. B* **92**, 241108 (2015).
14. A. Kitaev, *Ann. Phys*. **321**, 2 (2006).
15. W. Witczak-Krempa, G. Chen, Y.B. Kim, and L. Balents, *Annu. Rev. Condens. Matter Phys*. **5**, 57 (2014).
16. I. Kimchi, J.G. Analytis, and A. Vishwanath, *Phys. Rev. B* **90**, 205126 (2014).
17. V.N. Antonov, S. Uba, and L. Uba, *Phys. Rev. B* **98**, 245113 (2018).
18. M.Z. Hasan and C.L. Kane, *Rev. Mod. Phys*. **82**, 3045 (2010).
19. L. Balents, *Nature* **464**, 199 (2010).

20. T.-H. Han, J.S. Helton, S. Chu, D.G. Nocera, J.A. Rodriguez-Rivera, C. Broholm, and Y.S. Lee, *Nature* **492**, 406 (2012).
21. S.M. Albrecht, A.P. Higginbotham, M. Madsen, F. Kuemmeth, T.S. Jespersen, J. Nygrd, P. Krogstrup, and C.M. Marcus, *Nature* **531**, 206 (2016).
22. S.M. Winter, A.A. Tsirlin, M. Daghofer, J. van den Brink, Y. Singh, P. Gegenwart, and R. Valenti, *J. Phys.: Condens. Matter* **29**, 493002 (2017).
23. R. Schaffer, E.K.-H. Lee, B.-J. Yang, and Y.B. Kim, *Rep. Prog. Phys.* **79**, 094504 (2016).
24. R. Yadav, S. Rachel, L. Hozoi, J. van den Brink, and G. Jackeli, *Phys. Rev. B* **98**, 121107(R) (2018).
25. I. Kawasaki, S. Ogata, S. Kawai, Y. Fukuyama, A. Yamaguchi, and A. Sumiyama, *J. Phys. Soc. Jpn.* **87**, 014703 (2018).
26. S. Sachdev, *Quantum Phase Transitions*, Cambridge University Press, Cambridge, U.K. (1999).
27. G.R. Stewart, *Rev. Mod. Phys.* **73**, 797 (2001).
28. Y. Muro, N. Takeda, and M. Ishikawa, *J. Alloys Comp.* **257**, 23 (1997).
29. S. Araki, N. Metoki, A. Galatanu, E. Yamamoto, A. Thamizhavel, and Y. Onuki, *Phys. Rev. B* **68**, 024408 (2003).
30. P. Logg, Z. Feng, T. Ebihara, Y. Zou, S. Friedemann, P. Alireza, S. Goh, and F.M. Grosche, *Phys. Status Solidi B* **250**, 515 (2013).
31. V.A. Sidorov, E.D. Bauer, N.A. Frederick, J.R. Jeffries, S. Nakatsuji, N.O. Moreno, J.D. Thompson, M.B. Maple, and Z. Fisk, *Phys. Rev. B* **67**, 224419 (2003).
32. Y. Inada, A. Thamizhavel, H. Yamagami, T. Takeuchi, Y. Sawai, S. Ikeda, H. Shishido, T. Okubo, M. Yamada, K. Sugiyama, *et al.*, *Philos. Mag.* **82**, 1867 (2002).
33. K.D. Myers, S.L. Bud'ko, V.P. Antonov, B.N. Harmon, P.C. Canfield, and A.H. Lacerda, *Phys. Rev. B* **60**, 13371 (1999).
34. E. Jobiliong, J.S. Brooks, E.S. Choi, H. Lee, and Z. Fisk, *Phys. Rev. B* **72**, 104428 (2005).
35. Y. Saitoh, H. Fujiwara, T. Yamaguchi, Y. Nakatani, T. Mori, H. Fuchimoto, T. Kiss, A. Yasui, J. Miyawaki, S. Imada, *et al., J. Phys. Soc. Jpn.* **85**, 114713 (2016).
36. T. Takeuchi, A. Thamizhavel, T. Okubo, M. Yamada, N. Nakamura, T. Yamamoto, Y. Inada, K. Sugiyama, A. Galatanu, E. Yamamoto, *et al., Phys. Rev. B* **67**, 064403 (2003).
37. G.Y. Guo, H. Ebert, W.M. Temmerman, and P.J. Durham, *Phys. Rev. B* **50**, 3861 (1994).
38. V.N. Antonov, A.I. Bagljuk, A.Y. Perlov, V.V. Nemoshkalenko, V.N. Antonov, O.K. Andersen, and O. Jepsen, *Fiz. Nizk. Temp.* **19**, 689 (1993) [*Low Temp. Phys.* **19**, 494 (1993)].
39. V. Antonov, B. Harmon, and A. Yaresko, *Electronic Structure and Magneto-Optical Properties of Solids*, Kluwer, Dordrecht (2004).
40. E. Arola, M. Horne, P. Strange, H. Winter, Z. Szotek, and W.M. Temmerman, *Phys. Rev. B* **70**, 235127 (2004).
41. B.T. Thole and G. van der Laan, *Phys. Rev. B* **38**, 3158 (1988).
42. B.T. Thole, P. Carra, F. Sette, and G. van der Laan, *Phys. Rev. Lett.* **68**, 1943 (1992).
43. P. Carra, B.T. Thole, M. Altarelli, and X. Wang, *Phys. Rev. Lett.* **70**, 694 (1993).
44. B.T. Thole and G. van der Laan, *Phys. Rev. Lett.* **70**, 2499 (1993).
45. G. van der Laan and B.T. Thole, *Phys. Rev. B* **53**, 14458 (1996).
46. G. van der Laan, *Phys. Rev. B* **57**, 112 (1998).
47. V.N. Antonov, O. Jepsen, A.N. Yaresko, and A.P. Shpak, *J. Appl. Phys.* **100**, 043711 (2006).
48. V.N. Antonov, B.N. Harmon, A.N. Yaresko, and A.P. Shpak, *Phys. Rev. B* **75**, 184422 (2007).
49. V.N. Antonov, A.N. Yaresko, and O. Jepsen, *Phys. Rev. B* **81**, 075209 (2010).
50. O.K. Andersen, *Phys. Rev. B* **12**, 3060 (1975).
51. A.Y. Perlov, A.N. Yaresko, and V.N. Antonov, *PY-LMTO, A Spin-polarized Relativistic Linear Muffin-tin Orbitals Package for Electronic Structure Calculations*, (1995), unpublished.
52. V.V. Nemoshkalenko, A.E. Krasovskii, V.N. Antonov, Vl.N. Antonov, U. Fleck, H. Wonn, and P. Ziesche, *Phys. Status Solidi B* **120**, 283 (1983).
53. J.P. Perdew, K. Burke, and M. Ernzerhof, *Phys. Rev. Lett.* **77**, 3865 (1996).
54. P.E. Blöchl, O. Jepsen, and O.K. Andersen, *Phys. Rev. B* **49**, 16223 (1994).
55. A.N. Yaresko, V.N. Antonov, and P. Fulde, *Phys. Rev. B* **67**, 155103 (2003).
56. V.I. Anisimov and O. Gunnarsson, *Phys. Rev. B* **43**, 7570 (1991).
57. I.V. Solovyev, P.H. Dederichs, and V.I. Anisimov, *Phys. Rev. B* **50**, 16861 (1994).
58. P.H. Dederichs, S. Blügel, R. Zeller, and H. Akai, *Phys. Rev. Lett.* **53**, 2512 (1984).
59. W.E. Pickett, S.C. Erwin, and E.C. Ethridge, *Phys. Rev. B* **58**, 1201 (1998).
60. M. Cococcioni and S. de Gironcoli, *Phys. Rev. B* **71**, 035105 (2005).
61. K. Nakamura, R. Arita, Y. Yoshimoto, and S. Tsuneyuki, *Phys. Rev. B* **74**, 235113 (2006).
62. F. Aryasetiawan, M. Imada, A. Georges, G. Kotliar, S. Biermann, and A.I. Lichtenstein, *Phys. Rev. B* **70**, 195104 (2004).
63. I.V. Solovyev and M. Imada, *Phys. Rev. B* **71**, 045103 (2005).
64. V.P. Antropov, V.N. Antonov, L.V. Bekenov, A. Kutepov, and G. Kotliar, *Phys. Rev. B* **90**, 054404 (2014).
65. F. Aryasetiawan, K. Karlsson, O. Jepsen, and U. Schonberger, *Phys. Rev. B* **74**, 125106 (2006).
66. J.L. Campbell and T. Parr, *At. Data Nucl. Data Tables* **77**, 1 (2001).
67. T. Arakane, T. Sato, S. Souma, T. Takahashi, Y. Watanabe, and Y. Inada, *J. Magn. Magn. Mater.* **310**, 396 (2007).
68. Y. Inada, A. Tamizabel, Y. Sawai, S. Ikeda, H. Shishido, T. Okubo, M. Yamada, and Y. Onuki, *Acta Phys. Pol.* **34**, 1141 (2003).

69. D. Shoenberg, *Magnetic Oscillations in Metals*, Cambridge University Press, Cambridge (1984).
70. R. Prozorov, M.D. Vannette, G.D. Samolyuk, S.A. Law, S.L. Bud'ko, and P.C. Canfield, *Phys. Rev. B* **75**, 014413 (2007).
71. S.L. Bud'ko, S.A. Law, P.C. Canfield, G.D. Samolyuk, M.S. Torikachvili, and G.M. Schmiedeshoff, *J. Phys.: Condens. Matter* **20**, 115210 (2008).
72. J. Zaanen, G.A. Sawatzky, J. Fink, W. Speier, and J.C. Fuggle, *Phys. Rev. B* **32**, 4905 (1985).
73. J. Schwitalla and H. Ebert, *Phys. Rev. Lett.* **80**, 4586 (1998).
74. P. Krüger and C.R. Natoli, *Phys. Rev. B* **70**, 245120 (2004).
75. A.L. Ankudinov, A.I. Nesvizhskii, and J.J. Rehr, *Phys. Rev. B* **67**, 115120 (2003).

Електронна структура, поверхня Фермі та рентгенівський магнітний круговий дихроїзм в $CeAgSb_2$

В.М. Антонов

Електронна структура, поверхня Фермі, кутова залежність циклотронних мас та екстремальні перерізи поверхні Фермі, а також рентгенівський магнітний циркулярний дихроїзм (XMCD) в сполуці $CeAgSb_2$ було досліджено з перших принципів при використанні методу релятивістських лінійних muffin-tin орбіталей Дірака. У наших розрахунках Ce 4*f* стани розглядалися як: 1) делокалізовані, використовуючи узагальнене градієнтне наближення (GGA), 2) повністю локалізовані, розглядаючи їх як стани остовів, 3) частково локалізовані, з використанням наближення GGA+*U*. Розглянуто в деталях вплив спін-орбітальної взаємодії та кулонівського відштовхування *U* в рамках методу GGA+*U* на поверхню Фермі, орбітальну залежність циклотронних мас та екстремальні перерізи поверхні Фермі. Показано, що звичайне GGA наближення не описує поверхню Фермі $CeAgSb_2$ через неправильне енергетичне положення Ce 4*f* станів (розташовані занадто близько до енергії Фермі). Але з іншого боку, повністю локалізовані 4*f* стани та GGA+*U* наближення дають близький результат для поверхні Фермі та частоти dHvA у $CeAgSb_2$. Добре узгодження з експериментальними даними XMCD спектрів на краях поглинання Ce $M_{4,5}$ було отримано з використанням наближення GGA+*U*. Досліджено природу XMCD спектрів в сполуці, ефект дірки на остові в кінцевих станах з використанням наближення суперкомірки. Цей ефект покращує згоду між теорією та експериментом для XAS та XMCD спектрів на краях поглинання Ce $M_{4,5}$.

Ключові слова: поверхня Фермі, магнітний круговий дихроїзм, електронна структура.

Электронная структура, поверхность Ферми и рентгеновский магнитный циркулярный дихроизм в $CeAgSb_2$

В.Н. Антонов

Электронная структура, поверхность Ферми, угловая зависимость циклотронных масс и экстремальные сечения поверхности Ферми, а также рентгеновский магнитный циркулярный дихроизм (XMCD) в соединении $CeAgSb_2$ были исследованы из первых принципов с использованием метода релятивистских линейных muffin-tin орбиталей Дирака. В наших расчетах Ce 4*f* состояния рассматривались как: 1) делокализованные состояния, используя обобщенное градиентное приближение (GGA), 2) полностью локализованные, рассматривая их как состояния остовов, 3) частично локализованные, с использованием приближения GGA+*U*. Влияние спин-орбитального взаимодействия и кулоновского отталкивания *U* в рамках метода GGA+*U* на поверхность Ферми, орбитальную зависимость циклотронных масс и экстремальные сечения поверхности Ферми рассмотрено в деталях. Показано, что обычное GGA приближение не описывает поверхность Ферми $CeAgSb_2$ из-за неправильного энергетического положения Ce 4*f* состояний (расположены слишком близко к энергии Ферми). Но, с другой стороны, полностью локализованные 4*f* состояния и GGA+*U* приближение дает близкий результат для поверхности Ферми и частоты dHvA в $CeAgSb_2$. Хорошее согласие с экспериментальными данными по XMCD спектрам на краях поглощения Ce $M_{4,5}$ было получено с использованием приближения GGA+*U*. Исследована природа XMCD спектров в соединении, эффект дырки остова в конечных состояниях с использованием приближения суперячейки. Этот эффект улучшает согласие между теорией и экспериментом для XAS и XMCD спектров на краях поглощения Ce $M_{4,5}$.

Ключевые слова: поверхность Ферми, магнитный циркулярный дихроизм, электронная структура.